

Human Movement Modeling to Detect Biosignal Sensor Failures for Myoelectric Assistive Robot Control

Jun-ichiro Furukawa, *Member, IEEE*, Tomoyuki Noda, *Member, IEEE*, Tatsuya Teramae, and Jun Morimoto, *Member, IEEE*

Abstract—In this study, we propose a human movement model both for myoelectric assistive robot control and biosignal-sensor-failure detection. We particularly consider an application to upper extremity exoskeleton robot control. When using electromyography (EMG)-based assistive robot control, EMG electrodes can be easily disconnected or detached from skin surfaces because the human body is always in contact with the robot. If multiple electrodes are used to estimate multiple joint movements, the probability of sensor electrode misplacement increases due to human error. To cope with the aforementioned issues, we propose a novel human movement estimation model that takes anomalies into account as uncertain observations. We estimated human joint torques by automatically modulating the contribution of each sensor channel for the movement estimation based on anomaly scores that were computed according to synergistic muscular coordination. We compared our proposed method with conventional approaches during drinking-movement estimation with five healthy subjects in the three aforementioned anomaly situations and showed the effectiveness of our proposed method. We applied it to a four-DOF upper limb assistive exoskeleton robot and showed proper control in sensor failure situations.

Index Terms—Anomaly detection, electromyography (EMG), exoskeleton robot, human movement modeling, latent state estimation.

I. INTRODUCTION

DUE to the rapid progress of robotics technologies, robots are now expected to physically interact with humans and

Manuscript received February 17, 2016; revised November 24, 2016; accepted February 4, 2017. Date of publication April 24, 2017; date of current version August 7, 2017. This paper was recommended for publication by Associate Editor D. Kulic and Editor A. Kheddar upon evaluation of the reviewers' comments. This research was supported by the SRPBS from the Japan Agency for Medical Research and Development, AMED, and the "Research and development of technology for enhancing functional recovery of elderly and disabled people based on non-invasive brain imaging and robotic assistive devices," which is commissioned research of National Institute of Information and Communications Technology (NICT), Japan. Part of this research was supported by MIC-SCOPE, NEDO, Tateishi Science and Technology Foundation, JSPS KAKENHI Grant JP16H06565, JSPS KAKENHI Grant 15H05321, JSPS KAKENHI Grant 26820090, and the ImPACT Program of Council for Science, Technology and Innovation (Cabinet Office, Government of Japan).

The authors are with the Department of Brain Robot Interface, ATR computational Neuroscience Labs, Kyoto 619-0288, Japan (e-mail: furukawa@atr.jp; tomoyuki.noda@gmail.com; t-teramae@atr.jp; xmorimo@atr.jp).

This paper has supplementary downloadable material available at <http://ieeexplore.ieee.org>.

Color versions of one or more of the figures in this paper are available online at <http://ieeexplore.ieee.org>.

Digital Object Identifier 10.1109/TRO.2017.2683522

support their activities in industry and daily life. As a concrete application, using robotics technologies for the development of exoskeleton robots [1] or prosthetic devices [2] is becoming an important research direction, partly because many countries are facing aging populations.

For assistive devices, gaining the ability to detect human movement intentions from a user's biosignals is important. As one example of a biosignal, electromyography (EMG) has been widely used in previous studies. For example, investigations have been made into robots for EMG-based prostheses and exoskeletons [3]–[8].

For these EMG-based assistive devices, multiple electrodes must be used to estimate multiple joint movements for assistive robot control [10], [11]. However, when we consider using EMG-based assistive robot control in real-world applications, EMG sensor electrodes might easily become disconnected or detached from skin surfaces because human bodies are always in physical contact with the robot. In addition, sensor electrode misplacement due to human error is more likely when using multiple channels. Such sensor anomaly leads to significant errors in the estimation of a user's joint movements and causes robot uncontrollability.

Previous studies in the biomedical engineering field proposed fault detection methods for EMG sensors to address these failure situations. Most focused on independently monitoring the information of each EMG signal to identify faulty sensors [12]–[15]. For example, each sensor signal's variance was monitored [12]. However, since the variance may not always increase when a sensor anomaly occurs, this method can only be used for a limited number of fault situations. Other sensor fault detection methods might not be suitable for online robot control since they need a long monitoring period of the EMG signal sequence [13], careful tuning of the threshold to define the fault state [14], and prior knowledge of its fault state [15].

In our previous study, we explored a supervised learning method with logistic regression for sensor fault detection in a four-channel EMG system [16]. In this approach, the threshold was determined by the learning method. However, its scalability was limited since we needed to prepare every possible sensor failure situation to train the supervised learning method. Our previous method worked well with just a few sensor channels. However, when we used too many sensor channels, it was almost impossible to collect data in advance from every possible

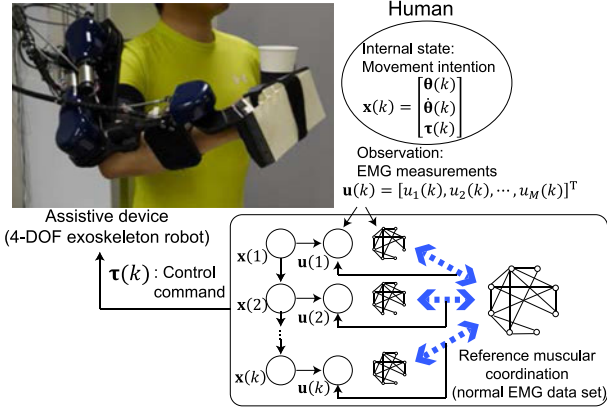


Fig. 1. Schematic diagram of the proposed human movement model that explicitly considers possibility of EMG-sensor failure occurrence. In this model, latent variable \mathbf{x} , representing the internal state, is estimated from observed EMG signals. Arrows from \mathbf{x} to \mathbf{u} indicate that EMG signals \mathbf{u} are essentially generated from movement intention \mathbf{x} . We adopted graphical model representation [9]. Estimated joint torques ($\boldsymbol{\tau}$), represented in internal state (\mathbf{x}), control an assistive robot while EMG signals (\mathbf{u}) are observed. We used deviation of measured correlation among all EMG sensor channels from proper muscular coordination to detect anomalies in EMG sensor channels.

sensor failure situation because the number of combinations of so many sensor channels was extremely large. We also needed to derive different controllers for each sensor failure situation since the input channels (from which the control inputs are derived) were identified in our previous method. For these reasons, we need a fundamentally different approach to cope with possible failure situations with many sensor channels.

In this paper, we propose a human movement model to cope with biosignal sensor failures while estimating joint torque from myoelectric signals. In fact, using dynamics models to detect anomaly situations is a common approach in the machine learning community [17].

Most previous EMG-based control studies considered EMG signals to be the user control commands, and the user commands of EMG signals are converted to the robot's joint movements by a linear conversion model [7], [8] or a nonlinear neural network model [10], [18]. In this study with a human movement model, we consider EMG signals to be observation variables and estimate the user's intended movements from observations (see Fig. 1). By framing the EMG-based control problem as an estimation problem of the user's movement intentions from the observed EMG signals, we can handle sensor failure situations as sensor noise problems. We propose a human movement estimation model that takes uncertain observations into account. Sensor anomaly detection and joint torque estimation are combined by exploiting human muscular synergistic coordination measured from multiple EMG electrodes.

In our preliminary study [19], we estimated one-DOF human joint movements using human muscular coordination to control a one-DOF external robot device, even under sensor failure situations. In this study, we show for the first time that a four-DOF, upper limb exoskeleton robot [20] can be controlled by the estimated joint torque from our proposed human movement model. 16-channel EMG electrodes were used to ob-

serve multiple muscle activities. As a concrete task, five healthy subjects performed a drinking motion in which we artificially disconnected the EMG electrodes or detached one side of an EMG probe from the skin surface. In addition, we intentionally misplaced two of the EMG electrodes in the 16-channel and tested every possible combination. Such anomaly situations are difficult to detect because the sensor signals seem normal and might cause significant estimation error.

The rest of this paper is organized as follows. In Section II, we introduce our human movement model with an anomaly detection method. Section III explains the experimental setup and the exoskeleton robot controller based on the estimated joint torque. Section IV shows the experimental results. We present performance results on anomaly detection, joint torque estimation compared with conventional sensor failure recovery methods, and online control performance on a 4-DOF exoskeleton assist robot by five healthy subjects. In each result, our proposed method has higher fault tolerability against all of the sensor anomaly situations considered in this study than other conventional methods. In Section V, we discuss the model selection problem and the limitations of our proposed method. Finally, we conclude in Section VI.

II. PROPOSED APPROACH

In our movement estimation approach, we used a movement model composed of forward body dynamics, a torque pattern generation model, and an EMG-signal observation model. We assume that the joint movement intention is represented as a sequence of joint torques. Later, we explain how we combine these three models to estimate user movement intention.

A. Body Dynamics and Torque Pattern Generation Models

1) *Forward Body Dynamics*: As presented in Fig. 1, we consider joint angle θ , angular velocity $\dot{\theta}$, and joint torque τ as the internal state of a human movement model: $\mathbf{x}(k) = [\boldsymbol{\theta}^\top(k), \dot{\boldsymbol{\theta}}^\top(k), \boldsymbol{\tau}^\top(k)]^\top$. As part of the human movement model, we consider forward body dynamics with first-order approximation as

$$\begin{aligned} \begin{bmatrix} \boldsymbol{\theta}(k+1) \\ \dot{\boldsymbol{\theta}}(k+1) \end{bmatrix} &= \begin{bmatrix} \boldsymbol{\theta}(k) \\ \dot{\boldsymbol{\theta}}(k) \end{bmatrix} \\ &+ \begin{bmatrix} \dot{\boldsymbol{\theta}}(k) \\ \mathbf{M}^{-1}(\boldsymbol{\theta}(k)) \left(-\mathbf{F}(\boldsymbol{\theta}(k), \dot{\boldsymbol{\theta}}(k)) \dot{\boldsymbol{\theta}}(k) - \mathbf{G}(\boldsymbol{\theta}(k)) \right) \end{bmatrix} \Delta t \\ &+ \begin{bmatrix} 0 \\ \mathbf{M}^{-1}(\boldsymbol{\theta}(k)) \end{bmatrix} \boldsymbol{\tau}(k) \Delta t \\ &+ \begin{bmatrix} \mathbf{w}_\theta(\mathbf{k}) \\ \mathbf{w}_{\dot{\theta}}(k) \end{bmatrix} \end{aligned} \quad (1)$$

where \mathbf{M} is the inertia matrix, \mathbf{F} is the centripetal coriolis, and \mathbf{G} is the gravity force, all of which can be derived from the identified exoskeleton robot parameters and the knowledge of human body parameters [21]. \mathbf{w}_θ and $\mathbf{w}_{\dot{\theta}}$ represent system noise that can also be used to cope with modeling errors. Δt is the sampling time.

2) *Torque Pattern Generation Model*: Since we use linear dynamics as the pattern generation model

$$\boldsymbol{\tau}(k+1) = \mathbf{A} \begin{bmatrix} \boldsymbol{\theta}(k) \\ \dot{\boldsymbol{\theta}}(k) \end{bmatrix} + \mathbf{B}\boldsymbol{\tau}(k) + \mathbf{w}_\tau(k) \quad (2)$$

the overfitting problem can be more effectively avoided while the model can represent movement trajectories better than the constant model, which was frequently used for estimating parameters in a state estimation model. However, the model complexity can be selected based on the purpose of a target task. Model parameters \mathbf{A} and \mathbf{B} can be derived from the measured motion profiles. Joint torque profiles that identify these parameters are derived from the inverse dynamics of a subject and a robot. These parameters were identified individually for each subject in an identification procedure that took less than a minute.

B. Observation Model

As presented in Fig. 1, processed EMG signals u in (4) are the observation variables of a human movement model

$$\mathbf{u}(k) = \mathbf{C}\mathbf{x}(k) + \mathbf{v}(k) \quad (3)$$

where \mathbf{C} is an observation matrix and \mathbf{v} represents the observation noise. We used a linear observation model since previous studies found that processed EMG signals can have a linear relationship with joint torque [7], [8], [11]. In addition, we discuss the suitability of linear models for our experimental setups using Akaike Information Criteria (AIC) in Section V. Processed EMG signals $\mathbf{u}(k) = [u_1(k), u_2(k), \dots, u_i(k), \dots, u_M(k)]^\top$ are observed using M EMG channels. Each channel observation u_i is calculated from i th EMG signal e_i by considering nonlinearity [22]

$$u_i = \frac{\exp(\alpha e_i) - 1}{\exp(\alpha) - 1} \quad (4)$$

where e_i is the full-wave rectified and low-pass-filtered signals of raw EMG signal z_i .

Observation matrix \mathbf{C} in (3) and nonlinear shape factor α in (4) are optimized to minimize the following cost function: $\sum_k (\mathbf{u}(k) - \mathbf{C}\mathbf{x}(k))^2$, where $\mathbf{x} = [\theta^\top, \dot{\theta}^\top, \tau^\top]^\top$ is the measured motion profiles for finding the model parameters and τ , as in previous studies [8], [18], [23], which were computed from the inverse dynamics of the arms of the subject and robot.

In this study, we design covariance $\mathbf{R}(k)$ of observation noise $\mathbf{v}(k) \sim \mathcal{N}(0, \mathbf{R}(k))$ in (3) so that the observation model can treat sensor failure situations. The covariance is represented as

$$\mathbf{R}(k) = \begin{pmatrix} \sigma_{e_1} + a_1\sigma_a & & \cdots & 0 \\ & \ddots & & \vdots \\ & & \sigma_{e_i} + a_i\sigma_a & \\ \vdots & & & \ddots \\ 0 & \cdots & & & \sigma_{e_M} + a_M\sigma_a \end{pmatrix}. \quad (5)$$

Here, σ_a indicates the basis noise variance that represents the uncertainty from the sensor failure. The size of the uncertainty is scaled with anomaly score a_i of the i th channel, where the anomaly score is calculated by monitoring the muscular coordination introduced in the next subsection. In this study, we simply set $\sigma_a = 1$, while this parameter could be optimized. σ_{e_i} is the observation noise variance of each EMG sensor channel without sensor failure situations.

C. Anomaly Score Calculation

Next, we introduce how we utilized human muscular coordination to detect sensor anomalies.

1) *Synergistic Muscular Coordination*: To some extent, since muscle activities generate similar patterns in identical motions [24], the muscular coordination patterns measured from multiple EMG electrodes retain nearly identical shapes during similar motions if all the sensors are normal. Therefore, we can detect the fault EMG sensors by monitoring the deterioration of the synergistic muscular coordination that they caused. In this study, we captured muscular coordination by the covariance among multiple muscle activations measured by EMGs. Given EMG sensor dataset \mathcal{D} as follows

$$\mathcal{D} = \{\mathbf{z}(k) | \mathbf{z}(k) \in \mathbb{R}^M, k = 1, 2, \dots, N\} \quad (6)$$

where N denotes the number of samples and M denotes the number of sensor channels, i.e., $\mathbf{z} = [z_1, z_2, \dots, z_M]^\top$. z_i is the standardized raw EMG signals measured by the i th channel. The muscular coordination can be stochastically represented by M -dimensional Gaussian distribution

$$\mathcal{N}(\mathbf{z}|0, \boldsymbol{\Lambda}^{-1}) = \frac{|\boldsymbol{\Lambda}|^{1/2}}{(2\pi)^{M/2}} \exp\left(-\frac{1}{2}\mathbf{z}^\top \boldsymbol{\Lambda} \mathbf{z}\right) \quad (7)$$

where $\boldsymbol{\Lambda} \in \mathbb{R}^{M \times M}$ represents a precision matrix, which is the inverse matrix of a covariance, and $|\boldsymbol{\Lambda}|$ denotes the determinant of $\boldsymbol{\Lambda}$.

2) *Anomaly Score*: The degree of sensor failure is represented by the anomaly score of each EMG channel. Here, we introduce how to calculate anomaly score a_i in (5). The difference between datasets \mathcal{D} and $\bar{\mathcal{D}}$ in terms of the i th sensor channel is measured by the Kullback–Leibler (KL) divergence of probabilistic models [25]

$$d_i^{\mathcal{D}\bar{\mathcal{D}}} \equiv \int p_{\bar{\mathcal{D}}}(\mathbf{h}_i) \int p_{\mathcal{D}}(z_i | \mathbf{h}_i) \ln \frac{p_{\bar{\mathcal{D}}}(z_i | \mathbf{h}_i)}{p_{\mathcal{D}}(z_i | \mathbf{h}_i)} dz_i d\mathbf{h}_i \quad (8)$$

where $\mathbf{h}_i = [z_1, \dots, z_{i-1}, z_{i+1}, \dots, z_M]^\top$, and the conditional probabilities are modeled as multivariate Gaussian distribution. Another measure, $d_i^{\mathcal{D}\bar{\mathcal{D}}}$, can be obtained by replacing \mathcal{D} with $\bar{\mathcal{D}}$ in the aforementioned. In this study, $\bar{\mathcal{D}}$ represents the reference data measured without a sensor fault. On the other hand, \mathcal{D} represents the newly observed data. Then, the anomaly score of the i th variable is defined as follows [25]:

$$a_i \equiv \max(d_i^{\mathcal{D}\bar{\mathcal{D}}}, d_i^{\bar{\mathcal{D}}\mathcal{D}}). \quad (9)$$

Using the aforementioned calculations, we derived the anomaly score, which was previously used (5). The calculation

method of KL divergence (8) from the observed EMG signals is explained in the Appendix.

D. Internal State Estimation

By combining the forward body dynamics model (1) and the torque pattern generation model (2), we can represent the movement model as an autonomous system, i.e., dynamics without explicit control input as

$$\mathbf{x}(k+1) = \mathbf{H}(\mathbf{x}(k)) + \mathbf{w}(k) \quad (10)$$

where $\mathbf{x}(k) = [\boldsymbol{\theta}^\top(k), \dot{\boldsymbol{\theta}}^\top(k), \boldsymbol{\tau}^\top(k)]^\top$ and $\mathbf{w} = [\mathbf{w}_\theta^\top, \mathbf{w}_{\dot{\theta}}^\top, \mathbf{w}_\tau^\top]^\top$. $\mathbf{w}(k) \sim \mathcal{N}(0, \mathbf{Q}(k))$ is the zero mean Gaussian system noise with \mathbf{Q} as its covariance. $\mathbf{H}(\mathbf{x})$ represents the internal state dynamics composed of functions (1) and (2).

Then, by considering the observation model introduced in (3), we can estimate the internal state with a state estimation method. For example, a Kalman filter was adopted to extract user motion intentions from brain activities [26], and the Bayesian method was used to estimate the human intentions [27]. We used the extended Kalman filter [28].

III. EXPERIMENTAL SETUPS

Here, we introduce our experimental setups with which we evaluate our proposed approach. First, we introduce our four-DOF, upper limb exoskeleton robot. Then, we explain our model parameter identification procedure and present experimental designs in the last two subsections. As a target task to evaluate our proposed method, we considered a drinking movement because it represents a common daily movement. We evaluated our proposed method with five healthy males (aged 24–32) who gave informed consent.

A. Four-DOF Upper Limb Exoskeleton Robot

The estimated joint torques are used to control our 4-DOF, upper limb exoskeleton robot actuated by pneumatic–electric (P-E) hybrid actuators [20]. As depicted in Fig. 2, the upper limb exoskeleton robot has four degrees of freedom: shoulder flexion/extension (SFE), shoulder abduction/adduction (SAA), elbow flexion/extension (EFE), and wrist flexion/extension (WFE) joints. Each joint torque τ_{PAM} is generated by a pneumatic artificial muscle (PAM), and the SFE and EFE joints are also actuated by electric motor output τ_{Motor} . The PAM unit has about 80–100-ms latency to generate the joint torques. This slow response is covered by the hybrid-driven electric motor in our current system. On the other hand, even without compensation by the electric motor, the latency of PAM control can be covered by EMG-based control because the EMG signals were activated to 60–100 ms prior to the actual limb movements [18]. The details of the mechanical design and the torque-based control method were previously presented [20].

B. Model Parameter Identification

We used a 4-DoF arm model for the forward body dynamics in (1), the inverse dynamics model that was used to acquire the torque pattern generation model in (2), and the observation

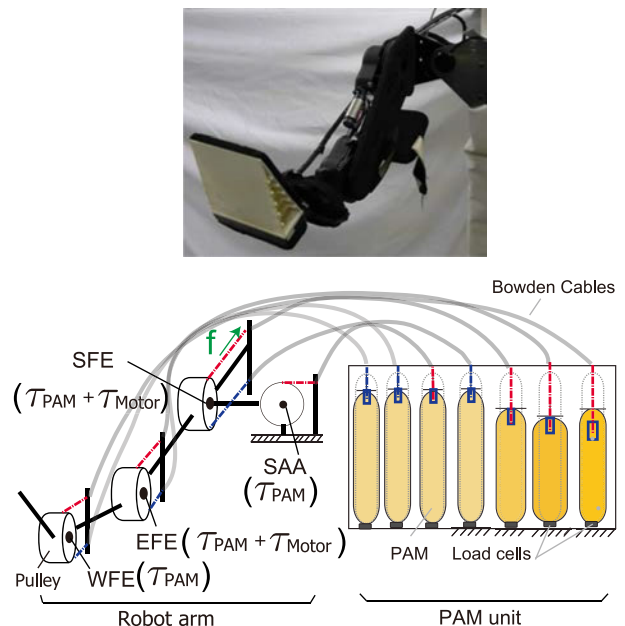


Fig. 2. Upper limb exoskeleton robot with four degrees of freedom: SFE, SAA, EFE, WFE. SFE and EFE joints are actuated by PAMs and electric motors. SAA and WFE joints are actuated by PAMs, located apart from joint and robot links. Each PAM force is transmitted to joints through Bowden cables and pulleys.

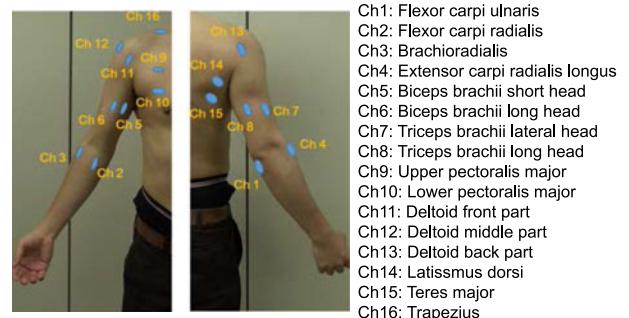


Fig. 3. EMG channel location. We used 16 channels to estimate 4-DOF joint movements.

model in (3). We first measured the subject’s body parameters, such as arm length and body weight. Then, we derived each link weight of the arm and the center of each link mass by plugging the body parameters into a formulation that was previously introduced [21]. We identified the weight of each robot link using a weight scale before we built the exoskeleton robot. We then added the identified robot link weights to the subject’s link weights where the center of the link mass (derived from the subject’s body parameter) was adopted to construct the arm model. We ignored the joint friction since our exoskeleton robot’s joints are highly backdrivable.

We measured the EMG signals from the right arms of the subjects as they generated a drinking motion while wearing the 4-DOF exoskeleton robot. These prerecorded drinking motion data for parameter identification were used to find the parameters of joint torque generators **A** and **B** in (2). We also used 16 Ag/AgCl bipolar surface EMG electrodes and measured the EMG signals from 16 muscles (see Fig. 3). The bipolar surface

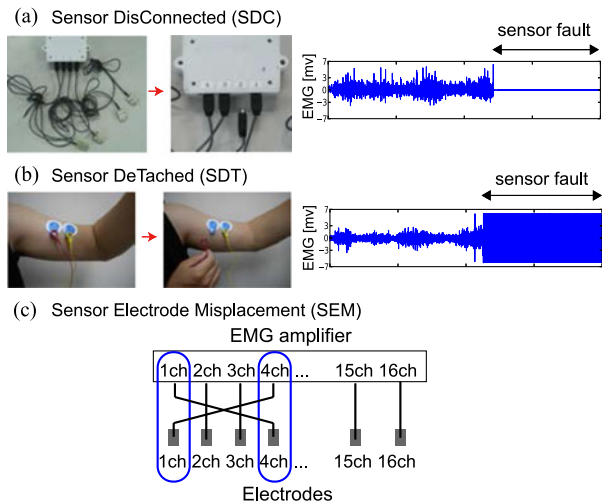


Fig. 4. Three types of sensor anomaly situations: (a) EMG electrode sensor is disconnected from amplifier; (b) one side of EMG electrode sensor is detached from skin surface; (c) two EMG electrodes in 16 channels are misplaced.

was 1-cm intervals along the longitudinal axis of the muscle's belly. Using the encoder of the 4-DOF exoskeleton robot system, we simultaneously recorded the SFE, the SAA, the EFE, and the WFE angle trajectories. The sampled EMG signals were low-pass filtered with a cutoff frequency of 2.6 Hz [29]. Then, the processed EMG signals were used to calibrate the observation model parameters C in (3) and α in (4). These model parameters were identified individually for each participant since the quantity of subcutaneous fat, skin impedance, and the way of using the muscles to generate movements can differ among users.

Validation results of the acquired model parameters are provided in Appendix C.

C. Sensor Anomaly Situations During Joint Torque Estimation

In this study, we consider three types of sensor anomaly conditions during the estimation of joint movements in drinking motions in two different experimental setups. First, we artificially made two types of sensor fault conditions when the subjects generated drinking motions. We disconnected the EMG electrode sensor from the amplifier and called this the SDC fault condition, and we detached one side of an EMG electrode sensor from the skin surface and called this the SDT fault condition [see Fig. 4(a) and (b)]. Second, we intentionally misplaced two EMG electrode connections in the 16 channels and called this anomaly the SEM condition [see Fig. 4(c)]. To validate our proposed method in the SEM condition, we tested all possible anomaly combinations (${}_{16}C_2 = 120$).

D. Online EMG-Based Assist Control

Fig. 5 shows a schematic diagram of an online upper limb exoskeleton control system. The exoskeleton robot is controlled based on the estimated SFE, SAA, EFE, and WFE joint torques of the subjects when they generate a drinking motion. The joint torques are simultaneously estimated from the measured EMG signals with our proposed method in which the anomaly scores were monitored. Then, the estimated joint torques are converted

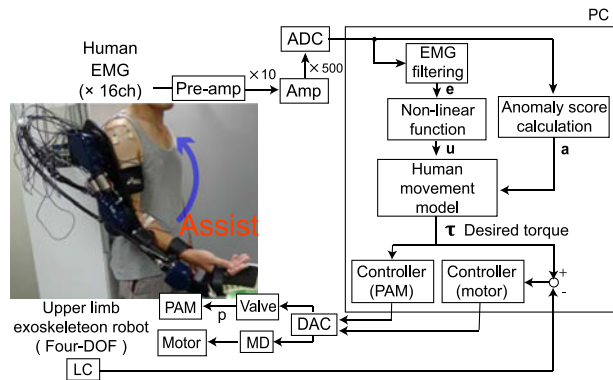


Fig. 5. Online EMG-based upper limb exoskeleton robot control.

to air pressure and electric current commands to drive the upper limb exoskeleton robot.

In our online robot control experiment, as an example, we chose the sixth and eleventh EMG channels as simultaneous SDC and SDT faults, where these channels mainly contributed to estimate the shoulder and elbow joint movements.

IV. RESULTS

In this section, we first compared the anomaly detection performance of our proposed method with the logistic regression method introduced in our previous study [16] and with a thresholding method in two simultaneous sensor fault conditions (SDC and SDT). Second, we compared the estimation performance of our proposed method with the threshold method against SEM anomaly situations. Finally, we showed the online assist control performance of an upper limb exoskeleton robot under sensor fault situations. In concrete, we compared the joint torque estimation performance of our proposed method with the standard method that has no sensor fault tolerability. Moreover, we compared the joint angle movements of our proposed method with those of the standard method in a drinking-movement generation task.

A. Anomaly Detection Performance

We compared the anomaly detection performances with five subjects in terms of the area under the curve (AUC). We used AUC for fair comparison since this value does not rely on the threshold setting. Fig. 6 compares the threshold, logistic regression, and our proposed methods. $AUC = 1.0$ means that the anomaly detection model is perfect; $AUC = 0.5$ means that the anomaly detection performance is chance level. We applied Welch's t -test adjusted by Bonferroni correction to the AUC of the logistic regression and the threshold method with reference to our proposed method. We found a significant difference between the proposed and logistic regression methods ($p < 0.05$ for SDC and SDT) and the threshold method ($p < 0.01$ for SDC), but no significant difference between the proposed and threshold methods against SDT was observed.

The anomaly detection performance of the logistic regression method was lower than the proposed method in both the SDC and SDT conditions. This is because it was originally designed to

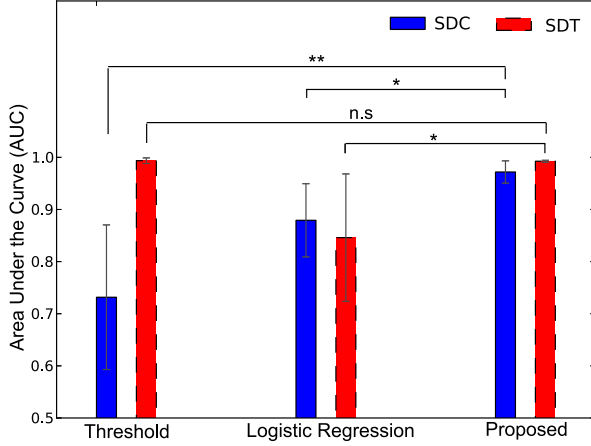


Fig. 6. Anomaly detection performance with five subjects: We compared AUCs of threshold, logistic regression, and our proposed methods against simultaneous SDC and SDT sensor fault conditions. AUC = 1.0 means that the anomaly detection model is perfect; AUC = 0.5 means that anomaly detection performance is chance level.

simply classify the normal condition and one particular anomaly situation. Therefore, using the logistic regression method is ineffective for detecting sensor failure situations in which more than one failure occurs at a time. Since logistic regression needs prior knowledge of all the possible anomaly states to prepare classifiers and estimation models to cope with anomaly situations, the scalability is also limited. The anomaly detection performance of the threshold method against the SDC fault condition is low, but the burst signals in the SDC fault condition are apparently easy to detect. Since the signal amplitude in the SDC condition is very low, simply classifying the normal rest state and the SDC condition with a threshold is difficult. These results show how effectively our proposed method detected simultaneous sensor faults.

On the other hand, in terms of efficiency, our proposed method took 2.1 ms to calculate one step, but the simple thresholding method only required 0.23 ms with a PC with an Intel(R) Core(TM) i7-3770K CPU at 3.5 GHz. Since our previous method failed to adequately cope with sensor failure situations with many sensor channels, we did not explicitly evaluate the computation burden. Although our proposed method needed a ten times longer calculation period than the simple thresholding method, 2.1 ms for one step calculation was fast enough for safely assisting human movements.

B. Joint Torque Estimation Performance

Here, we validate our proposed method of joint torque estimation performance in SEM anomaly situations. In SEM situations, we consider all possible anomaly state combinations in 16-channels (${}_{16}C_2 = 120$ patterns) for all five subjects. Since it is difficult to use the logistic regression method in this case (as explained in the previous subsection), we compared our proposed method with the threshold method. For the threshold method, we prepared two different torque estimation approaches: 1) *Threshold+SW* is a switching estimator approach that we also used in the logistic regression method in our

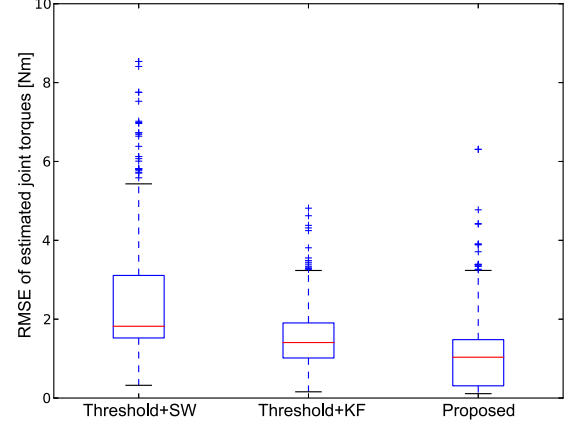


Fig. 7. Root mean squared errors (RMSE) between actual and estimated joint torques combining all joints (SFE, SAA, EFE, and WFE) using *Threshold+SW* method in which a reliable estimation model is selected based on anomaly detection by *Threshold+KF*. Joint torques are estimated by a Kalman filter, and equivalent values to the maximum anomaly scores are put into covariance $\mathbf{R}(k)$ when fault signals are detected by the threshold and our proposed method with five subjects against SEM sensor anomaly conditions. SEM sensor anomaly situations were tested in all possible combinations (${}_{16}C_2 = 120$ patterns) for each subject. Therefore, each boxplot includes data from 600 samples. Mann-Whitney test, adjusted by Bonferroni correction, was applied to three RMSEs; significant differences exist among them ($p < 0.01$).

previous study [16]; and 2) *Threshold+KF* is a Kalman filter approach that we also used in our proposed method, as explained in Section II.

In the threshold method, we first identified the minimum and maximum linear envelopes of the EMG signals from the data acquired in the normal condition. We used the minimum (β^{\min}) and maximum values (β^{\max}) of the linear envelope of the EMG signals as the upper and lower thresholds. We identified these thresholds for each channel, meaning that each channel has different upper and lower thresholds.

In the switching estimator approach, the torque estimators were switched based on the switching condition defined by the threshold as

$$\tau(k) = \begin{cases} \mathbf{K}_{-i} \mathbf{u}_{-i}(k) & (u_i < \beta_i^{\min} \text{ or } \beta_i^{\max} < u_i) \\ \mathbf{K}_{-i,-j} \mathbf{u}_{-i,-j}(k) & (u_i < \beta_i^{\min} \text{ or } \beta_i^{\max} < u_i \\ & (u_j < \beta_j^{\min} \text{ or } \beta_j^{\max} < u_j) \\ \mathbf{K}_{\text{all}} \mathbf{u}_{\text{all}}(k) & (\text{otherwise}). \end{cases} \quad (11)$$

Here, processed EMG signals \mathbf{u}_{-i} , $\mathbf{u}_{-i,-j}$ and \mathbf{u}_{all} are represented as

$$\begin{aligned} \mathbf{u}_{-i} &= [u_1, u_2, \dots, u_{i-1}, u_{i+1}, \dots, u_M]^\top \\ \mathbf{u}_{-i,-j} &= [u_1, u_2, \dots, u_{i-1}, u_{i+1}, \dots, u_{j-1}, u_{j+1}, \dots, u_M]^\top \\ \mathbf{u}_{\text{all}} &= [u_1, u_2, \dots, u_M]^\top \end{aligned} \quad (12)$$

where parameter vectors \mathbf{K}_{-i} , $\mathbf{K}_{-i,-j}$, and \mathbf{K}_{all} are derived from the training data used in Section III-B.

For the Kalman filter approach, we used the same framework introduced in Section II. Since no anomaly scores were provided in the threshold method, we manually designed corresponding constant value γ_i that is used in observation noise covariance \mathbf{R} instead of a_i in (5), where we set the constant

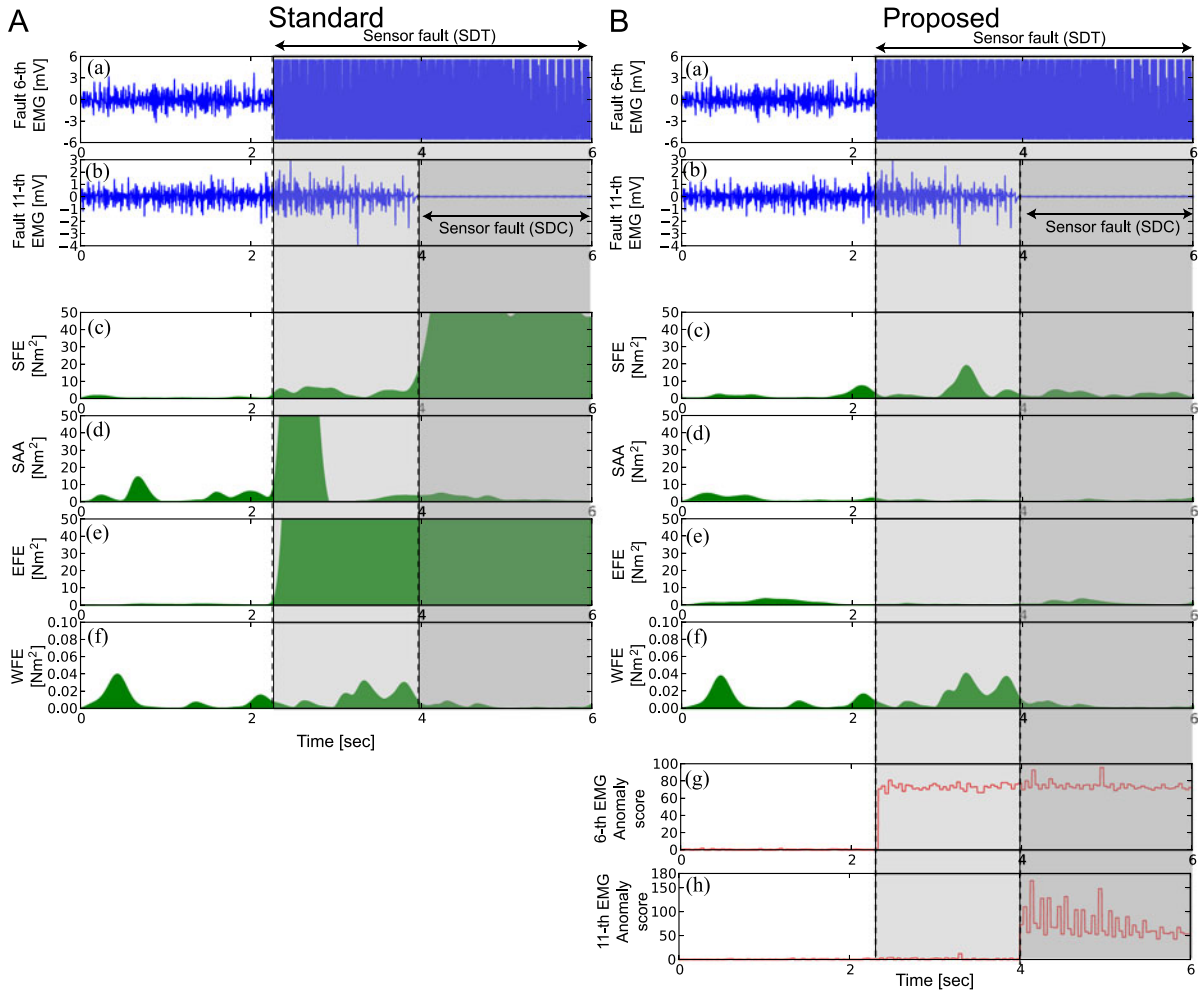


Fig. 8. Estimated joint torque performances of standard and proposed methods: (A) (a) and (b) and (B) (a) and (b) show raw fault EMG signals. (A) (c)–(f) and (B) (c)–(f) show squared errors between actual and estimated joint torques: SFE, SAA, EFE, and WFE. (B) (g) and (h) show anomaly scores of fault EMG signals (B) (a) and (b).

value to $\gamma_i = 0$ if the i th EMG signal state was within the normal range and to $\gamma_i = a_i^{\max}$ if the i th EMG signal amplitude was below lower threshold β_i^{\min} or above upper threshold β_i^{\max} . We identified the maximum anomaly score in SEM condition a_i^{\max} after we applied the proposed method. Therefore, this method somewhat used the prior knowledge provided by our proposed method. Note that this Kalman filter approach, i.e., using an extended Kalman filter as a torque estimation method while using the threshold method as an anomaly detector, is also a novel method.

Fig. 7 shows the torque estimation errors for all of the joints: SFE, SAA, EFE, and WFE. Against the SEM sensor anomaly situations, we compared the following three methods: 1) *Threshold+SW*; 2) *Threshold+KF*; and 3) the proposed method. Our proposed method's RMSE is lower than the two threshold methods. We applied the Mann–Whitney test, adjusted by Bonferroni correction to the three RMSEs, and found significant differences among them ($p < 0.01$). We show the torque estimation performances for each joint in Appendix (see Fig. 11). These results clearly emphasize the advantage of our proposed method.

C. Online EMG-Based Assist Control

In our online EMG-based robot control experiment, we compared our proposed method with a standard method without fault tolerability that always uses all of the EMG sensor channels to derive the joint torques. In the standard method, as in a previous work [7], [8], [11], we used the linear model to estimate the joint torque from the EMG signals of all of the EMG sensor inputs \mathbf{u}_{all} in (12) as

$$\boldsymbol{\tau}(k) = \mathbf{K}_{\text{all}} \mathbf{u}_{\text{all}}(k). \quad (13)$$

We applied both the standard method and our proposed method to the SDC and SDT sensor failure conditions.

Fig. 8 shows the estimated joint torque performances of the standard and proposed methods for one of the five subjects. (A) (a) and (b) and (B) (a) and (b) show the raw EMG signal profiles that include two types of sensor fault situations, SDT and SDC. (A) (c)–(f) show the squared errors between each estimated joint torque with the standard method and the actual joint torques, where the actual joint torques were derived from the inverse dynamics of a subject and the robot arms with the actual joint

TABLE I
RMSE OF ESTIMATED TORQUE FOR EACH JOINT USING
STANDARD AND PROPOSED METHODS

Subject	Joint	RMSE [Nm]			
		Normal Condition		Fault Condition	
		Standard	Proposed	Standard	Proposed
A	SFE	1.32	1.36	5.04	1.58
	SAA	0.658	0.795	2.45	1.00
	EFE	0.625	0.793	> 10	2.83
	WFE	0.135	0.121	0.178	0.128
B	SFE	1.35	1.13	2.06	1.79
	SAA	1.54	1.43	1.44	1.35
	EFE	1.15	0.930	2.23	0.951
	WFE	0.129	0.128	0.151	0.135
C	SFE	1.18	1.19	> 10	1.21
	SAA	1.34	1.03	1.88	0.995
	EFE	0.674	0.918	1.81	0.951
	WFE	0.120	0.148	0.149	0.136
D	SFE	1.07	0.748	>> 10	0.771
	SAA	0.767	0.671	0.792	0.660
	EFE	0.794	0.751	1.18	1.09
	WFE	0.138	0.110	0.131	0.127
E	SFE	0.926	0.741	>> 10	5.67
	SAA	0.534	0.492	1.00	0.567
	EFE	0.728	0.697	1.40	0.792
	WFE	0.223	0.237	0.251	0.235

trajectories. (B) (c)–(f) show the squared errors between each estimated joint torque with our proposed method and the actual joint torques. (B) (g) and (h) show the anomaly scores of the fault EMG channels. (B) (a) corresponds to SDT, and (B) (b) corresponds to SDC.

As shown in Fig. 8 (A) (c)–(f), the large errors of the standard method during the sensor fault condition degraded the estimation performances. On the other hand, from (B) (c)–(f) in Fig. 8, the error of our proposed method was much smaller than the standard method and successfully estimated the joint torques even after sensor faults occurred.

Table I shows the RMSE between the actual and estimated torques for each joint with all five subjects using two different methods: the standard and our proposed methods during the normal condition and the trial period, which includes the sensor fault conditions. From Table I, the RMSEs of the standard method always exceeded those of the proposed method when the trials included the sensor failure periods. In the normal condition, the RMSEs of the standard method resembled those of the proposed method. However, in 13 of 20 cases, the proposed method showed better estimation performances even in the normal condition. Since we selected the sixth and eleventh EMG channels that contributed to estimate the SFE and EFE joint movements, large differences in the estimation performances between the standard and proposed methods can be observed in the SFE and EFE joints. The torque estimation performance of the SFE joint in subject E is worse than the others. This was because the actual signal measured by the failure channel happened to resemble the normal condition's signal. This situation was difficult to cope with in the failure detection methods.

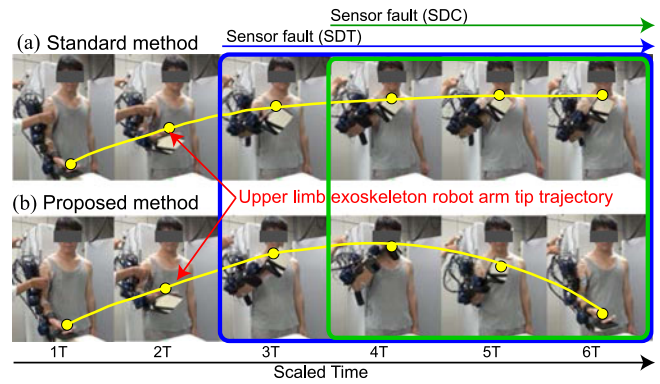


Fig. 9. Control performance of upper limb exoskeleton: (a) Standard method. Robot movement almost stopped after sensor failure occurrence. (b) Proposed method. Drinking motions were successfully generated with our proposed method even during sensor fault periods.

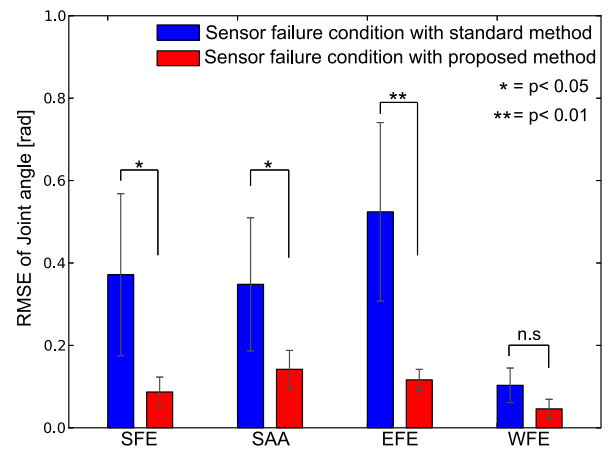


Fig. 10. Exoskeleton assist control performances of standard and proposed methods across all five subjects. Errors of our proposed method with sensor failures were smaller than the standard method.

Fig. 9 shows the control performance of our upper limb exoskeleton robot. When we used the standard method, the robot movement almost stopped after sensor failures. On the other hand, drinking motions were successfully generated with our proposed method even during sensor fault periods.

In Fig. 10, we show the joint angle estimation errors of the standard and proposed methods by comparing the control performance of our proposed method with that of the standard method in movement trials that include the sensor failure conditions. We also applied Welch's *t*-test to the RMSE of each joint and found significant differences: SFE ($p < 0.05$), SAA ($p < 0.05$), and EFE ($p < 0.01$). We found no significant differences in the WFE joint. The fault channel selected in this online experiment made a small contribution to the WFE torque estimation.

From these results, the standard method's errors were large when the movement trial periods included sensor faults. On the other hand, the control performances of our proposed method with the sensor failure periods were much better than those of the standard method. Some error remained even when we used our proposed method, partly due to the variations of the subjects' intended drinking movements (see Fig. 12 in

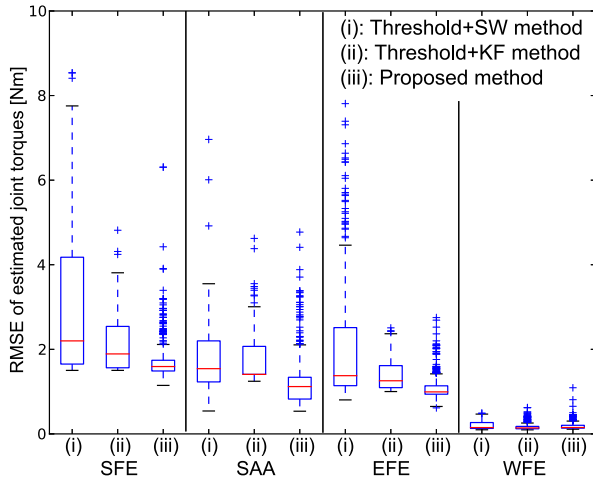


Fig. 11. RMSEs between actual and estimated joint torques of joints SFE, SAA, EFE, and WFE using *Threshold+SW*, *Threshold+KF*, and our proposed methods with five subjects against SEM sensor anomaly conditions.

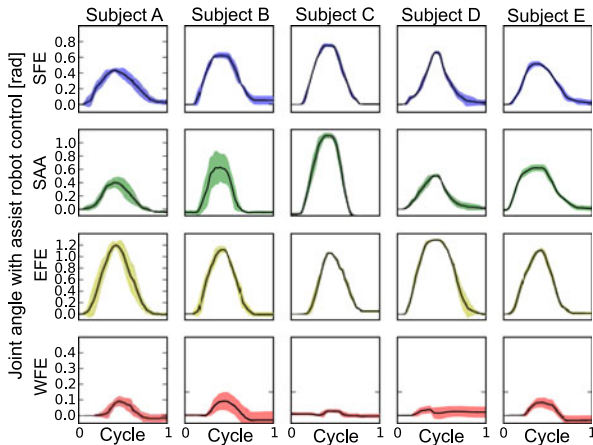


Fig. 12. Mean and standard deviation of joint trajectories generated from each subject without exoskeleton assist control during drinking motions.

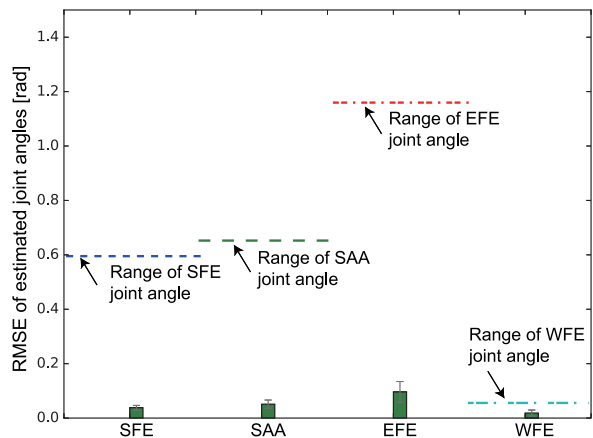


Fig. 13. RMSE of estimated joint angle trajectories with our proposed method without exoskeleton assist control during drinking motions. Average movement range of each joint angle of five subjects is also shown.

Appendix B). These results clearly show the advantage of using a human movement model for EMG-based assist robot control.

V. DISCUSSION

Although previous studies experimentally proved the suitability of using linear models to describe the relationships between joint torques and EMG signals, we further investigated the appropriateness of linear models in our experimental setups with the AIC to select models to describe the relationship. We found that first-order (linear) models were selected based on AIC in 58 out of 80, where we calculated the AIC for all the EMG profiles measured from all five subjects with all 16 sensor channels. These results suggest that using linear models is an appropriate approach to describe the mapping between joint torque and EMG.

The Kalman filter was also previously used [26] for estimating movement intentions from biological signals. However, that work [26] directly estimated the movements from the brain activities of monkeys, not EMGs measured from a human subject. Moreover, it did not deal with anomaly detection; our main claim is the usefulness of an internal model to cope with anomaly situations.

We considered three different types of anomaly situations. To the best of our knowledge, no proposed systematic approach can cope with all three types of anomalies. Therefore, coping with different failure situations with just one anomaly detection method seems crucial.

Although we used the Gaussian distribution model in (7), we do not aim to precisely identify EMG signal distribution; our goal is finding anomaly correlation structures. Therefore, EMG signals do not need to be Gaussian distributed, as empirically investigated [25], [30]. However, since muscular coordination (with which anomaly scores are calculated) can depend on target movements, we need to identify the synergistic muscle patterns for each one. To cope with this possible limitation, explicitly considering the dissimilarity of muscular coordination patterns [31] is an interesting future direction.

By scrutinizing the video of our experiments, we observed the movement delay of the exoskeleton robot during its downward arm motion. This might reflect the outgassing latency of the PAM of one side of the cocontracting air muscle system. If so, we might be able to fix this delay by carefully conducting system identification of the air muscle system by following our recent study [32]. Since we recorded the video during the normal sensor condition, this delay was not caused by the amplitude of the anomaly scores that affects the joint torque estimation process.

VI. CONCLUSION

We proposed a human movement model both for EMG-based assistive control and biosignal-sensor-failure detection. We combined the sensor anomaly detection and joint movement estimations by exploiting the human muscular coordination patterns measured from multiple EMG electrodes. Our proposed

model estimates the intended movements by observing EMG signals while uncertain observations were taken into account. To validate our proposed method, we used 16-EMG channels and a 4-DOF upper limb exoskeleton robot driven by estimated joint movements with five healthy subjects who performed a drinking motion. In this study, we considered three types of anomaly situations: 1) an EMG electrode disconnected from an amplifier (SDC) 2); an EMG channel detached from the skin surface (SDT); and 3) two EMG electrodes connections were misplaced (SEM).

Our proposed model successfully detected anomaly sensors and estimated the joint movements of the subjects. In addition, with our proposed method, five healthy subjects successfully controlled a 4-DOF upper limb exoskeleton robot to generate drinking motions even under two EMG sensor simultaneous fault conditions: SDC and SDT. Our results show the usefulness of a human movement model for EMG-based assistive control using multiple electrodes. We have already applied our proposed approach to a 1-DOF exoskeleton robot in a previous preliminary study [19] and a 4-DOF exoskeleton robot in Fig. 2. Therefore, our proposed approach is not specific to particular hardware. Our future study will apply our proposed method to other types of exoskeleton robots, such as lower limb exoskeleton robots [33], [34].

In addition, we will extend this approach to deal with a wider variety of movements with multiple sensor channels while deriving the parameters of a human movement estimation model from the data acquired from other people using our previously proposed transfer learning approach [35], [36]. Such transfer learning approaches could also be used to develop a user-independent biosignal sensor failure detection method.

APPENDIX A

Here, we introduce how to derive synergetic muscle coordination from the observed EMG data and the KL divergence between the reference and current muscle coordinations.

We assume that datasets \mathcal{D} have been standardized to have zero mean and unit variance. Then, empirical covariance matrix Σ of the EMG datasets is given as

$$\Sigma = \frac{1}{N} \sum_{k=1}^N \mathbf{z}(k) \mathbf{z}(k)^\top. \quad (14)$$

Next, we derive precision matrix Λ of the multivariate Gaussian in (7). However, since the sample covariance matrix is often rank deficient and no inverse exists, using a regularization method is necessary. As previously suggested [37], [38], we consider L_1 -norm regularization to find the sparse precision matrix by maximizing the objective function

$$\Lambda^* = \arg \max_{\Lambda} [\ln |\Lambda| - \text{tr}(\Sigma \Lambda) - \rho \|\Lambda\|_1]. \quad (15)$$

When the block coordinate descent algorithm is used for the objective function in (15) [37], [38], we focus on particular single channel z_i and set a partition for the precision matrix Λ

and its inverse as

$$\Lambda = \begin{pmatrix} \mathbf{L} & \mathbf{l} \\ \mathbf{l}^\top & \lambda \end{pmatrix}, \quad \Sigma \equiv \Lambda^{-1} = \begin{pmatrix} \mathbf{S} & \mathbf{s} \\ \mathbf{s}^\top & \sigma \end{pmatrix} \quad (16)$$

where the rows and columns are always arranged so that the z_i -related entries are set in the last row and the last column. Therefore, $\mathbf{L}, \mathbf{S} \in \mathbb{R}^{(M-1) \times (M-1)}$, $\lambda, \sigma \in \mathbb{R}$, and $\mathbf{l}, \mathbf{s} \in \mathbb{R}^{M-1}$.

Then, since we assume a Gaussian distribution, as in (7), expected KL divergence d_i can be computed [25] as

$$\begin{aligned} d_i^{\mathcal{D}} &= \bar{\mathbf{s}}^\top (\mathbf{l} - \bar{\mathbf{l}}) \\ &+ \frac{1}{2} \left\{ \frac{\mathbf{l}^\top \bar{\mathbf{S}} \mathbf{l}}{\lambda} - \frac{\bar{\mathbf{l}}^\top \bar{\mathbf{S}} \bar{\mathbf{l}}}{\bar{\lambda}} \right\} \\ &+ \frac{1}{2} \left\{ \ln \frac{\bar{\lambda}}{\lambda} + \bar{\sigma} (\lambda - \bar{\lambda}) \right\}. \end{aligned} \quad (17)$$

d_i , which measures the change in the neighborhood graph of the i th node, was used in (9).

APPENDIX B

Here, we compare the joint torque estimation errors for each joint against SEM anomaly situations in Fig. 11. In the SEM situations, we consider every possible anomaly state combination in the 16 channels (${}_{16}C_2 = 120$ patterns) for all five subjects.

We also show the mean and standard deviation of the joint angle trajectories freely generated from each subject without exoskeleton robot assist control in Fig. 12. We computed these trajectories with the data from four trials for each subject.

APPENDIX C

To validate the acquired dynamic model, we evaluated the errors between the estimated and measured joint angles during drinking movements. Since the joint angle estimation performance depends on the acquired dynamic model's validity, we validated its acquired parameters by evaluating the joint angle estimation errors. Fig. 13 shows the validation results. The RMSEs of each estimated joint angle are much smaller than the joint movement ranges. This result indicates that the model parameters were properly estimated.

REFERENCES

- [1] A. M. Dollar and H. Herr, "Lower extremity exoskeletons and active orthoses: Challenges and state-of-the-art," *IEEE Trans. Robot.*, vol. 24, no. 1, pp. 144–158, Feb. 2008.
- [2] A. Fougner, O. Stavdahl, P. Kyberd, Y. Losier, and P. Parker, "Control of upper limb prostheses: Terminology and proportional myoelectric control—A review," *IEEE Trans. Neural Syst. Rehabil. Eng.*, vol. 20, no. 5, pp. 663–677, Sep. 2012.
- [3] C. Castellini, A. E. Fiorilla, and G. Sandini, "Multi-subject / daily-life activity EMG-based control of mechanical hands," *J. Neuroeng. Rehabil.*, vol. 6, 2009. Art. no. 41.
- [4] C. K. Batty, A. Nightingale, and J. Whillis, "The use of myo-electric currents in the operation of prostheses," *J. Bone Joint Surg. Brit. Vol.*, vol. 37-B, no. 3, pp. 506–510, 1955.
- [5] K. Ha, H. Varol, and M. Goldfarb, "Volitional control of a prosthetic knee using surface electromyography," *IEEE Trans. Biomed. Eng.*, vol. 58, no. 1, pp. 144–151, Jan. 2011.

- [6] J. Ngeo *et al.*, "Control of an optimal finger exoskeleton based on continuous joint angle estimation from EMG signals," in *Proc. 35th Annu. Int. Conf. IEEE Eng. Med. Biol. Soc.*, Jul. 2013, pp. 338–341.
- [7] T. Lenzi, S. De Rossi, N. Vitiello, and M. Carrozza, "Intention-based EMG control for powered exoskeletons," *IEEE Trans. Biomed. Eng.*, vol. 59, no. 8, pp. 2180–2190, Aug. 2012.
- [8] C. Fleischer, C. Reinicke, and G. Hommel, "Predicting the intended motion with EMG signals for an exoskeleton orthosis controller," in *Proc. IEEE/RSJ Int. Conf. Intell. Robots Syst.*, Aug. 2005, pp. 2029–2034.
- [9] C. M. Bishop, *Pattern Recognition and Machine Learning (Information Science and Statistics)*. Secaucus, NJ, USA: Springer-Verlag, 2006.
- [10] K. Kiguchi and Y. Hayashi, "An EMG-based control for an upper-limb power-assist exoskeleton robot," *IEEE Trans. Syst., Man, Cybern. B, Cybern.*, vol. 42, no. 4, pp. 1064–1071, Aug. 2012.
- [11] J. Furukawa, T. Noda, T. Teramae, and J. Morimoto, "An EMG-driven weight support system with pneumatic artificial muscles," *IEEE Syst. J.*, vol. 10, no. 3, pp. 1026–1034, Sep. 2016.
- [12] N. M. Lopez, F. di Sciascio, C. M. Soria, and M. E. Valentinuzzi, "Robust EMG sensing system based on data fusion for myoelectric control of a robotic arm," *BioMed. Eng. Online*, vol. 8, 2009, Art. no. 5.
- [13] R. Halabi, M. Diab, B. Moslem, M. Khalil, and C. Marque, "Detecting missing signals in multichannel recordings by using higher order statistics," in *Proc. 34th Annu. Int. Conf. IEEE Eng. Med. Biol. Soc.*, San Diego, California, USA, Aug. 28–Sep. 1 2012, pp. 3110–3113.
- [14] X. Zhang *et al.*, "On design and implementation of neural-machine interface for artificial legs," *IEEE Trans. Ind. Informat.*, vol. 7, no. 5, pp. 418–429, May 2012.
- [15] H. Huang, F. Zhang, Y. L. Sun, and H. He, "Design of a robust EMG sensing interface for pattern classification," *J. Neural Eng.*, vol. 7, no. 5, 2010, Art. no. 056005.
- [16] J. Furukawa, T. Noda, T. Teramae, and J. Morimoto, "Fault tolerant approach for biosignal-based robot control," *Adv. Robot.*, vol. 29, no. 7, pp. 505–514, 2015.
- [17] M. Basseville and I. V. Nikiforov, *Detection of Abrupt Changes: Theory and Application*. Englewood Cliffs, NJ, USA: Prentice-Hall, 1993.
- [18] Y. Koike and M. Kawato, "Estimation of dynamic joint torques and trajectory formation from surface electromyography signals using a neural network model," *Biol. Cybern.*, vol. 73, no. 4, pp. 291–300, Sep. 1995.
- [19] J. Furukawa, T. Noda, T. Teramae, and J. Morimoto, "Estimating joint movements from observed EMG signals with multiple electrodes under sensor failure situations toward safe assistive robot control," in *Proc. IEEE Int. Conf. Robot. Autom.*, May 2015, pp. 4985–4991.
- [20] T. Noda, T. Teramae, B. Ugurlu, and J. Morimoto, "Development of an upper limb exoskeleton powered via pneumatic electric hybrid actuators with Bowden cable," in *Proc. IEEE/RSJ Int. Conf. Intell. Robots Syst.*, Sep. 2014, pp. 3573–3578.
- [21] D. A. Winter, *Biomechanics and Motor Control of Human Movement*. New York, NY, USA: Wiley, 2009.
- [22] J. Potvin, R. Norman, and S. McGill, "Mechanically corrected EMG for the continuous estimation of erector spinae muscle loading during repetitive lifting," *Eur. J. Appl. Physiol. Occup. Physiol.*, vol. 74, no. 1–2, pp. 119–132, 1996.
- [23] T. Noda, J. Furukawa, T. Teramae, and J. Morimoto, "An electromyogram based force control coordinated in assistive interaction," in *Proc. IEEE Int. Conf. Robot. Autom.*, Karlsruhe, Germany, May 2013, pp. 2657–2666, Paper WeC6.4.
- [24] Z. Li, G. D., and H. M., "Inverse estimation of multiple muscle activations from joint moment with muscle synergy extraction," *IEEE J. Biomed. Health Inform.*, vol. 19, no. 1, pp. 64–73, Jan. 2015.
- [25] T. Ide, A. C. Lozano, N. Abe, and Y. Liu, "Proximity-based anomaly detection using sparse structure learning," in *Proc. SIAM Int. Conf. Data Mining*, 2009, pp. 97–108.
- [26] W. Wu, Y. Gao, E. Bienenstock, J. P. Donoghue, and M. J. Black, "Bayesian population decoding of motor cortical activity using a Kalman filter," *Neural Comput.*, vol. 18, no. 1, pp. 80–118, Jan. 2006. [Online]. Available: <http://dx.doi.org/10.1162/089976606774841585>
- [27] C.-A. Cheng, T.-H. Huang, and H.-P. Huang, "Bayesian human intention estimator for exoskeleton system," in *Proc. IEEE/ASME Int. Conf. Adv. Intell. Mechatronics*, Jul. 2013, pp. 465–470.
- [28] F. L. Lewis, *Optimal Estimation: With an Introduction to Stochastic Control Theory*. New York, NY, USA: Wiley-Interscience, 1986.
- [29] M. Yoshida and M. Terao, "Suitable cutoff frequency of low-pass filter for estimating muscle force by surface electromyogram," in *Proc. 25th Annu. Int. Conf. IEEE Eng. Med. Biol. Soc.*, vol. 2, Sep. 2003, pp. 1709–1711.
- [30] T. Ide, "Sparse structure learning for correlation anomaly detection," (in Japanese), in *Proc. Japanese Soc. Artif. Intell. Workshop Data Mining Statistical Math.*, 2009, Art. no. SIG-DMSM-A803-04.
- [31] A. A. Samadani and D. Kulic, "Hand gesture recognition based on surface electromyography," in *Proc. 36th Annu. Int. Conf. IEEE Eng. Med. Biol. Soc.*, 2014, pp. 4196–4199.
- [32] B. Ugurlu, P. Forni, C. Doppmann, and J. Morimoto, "Torque and variable stiffness control for antagonistically driven pneumatic muscle actuators via a stable force feedback controller," in *Proc. IEEE/RSJ Int. Conf. Intell. Robots Syst.*, Sep. 2015, pp. 1633–1639.
- [33] S. Hyon, J. Morimoto, T. Matsubara, T. Noda, and M. Kawato, "XoR: Hybrid drive exoskeleton robot that can balance," in *Proc. IEEE/RSJ Int. Conf. Intell. Robots Syst.*, 2011, pp. 3975–3981.
- [34] B. Ugurlu, C. Doppmann, M. Hamaya, T. Teramae, T. Noda, and J. Morimoto, "Variable ankle stiffness improves balance control: Experiments on a bipedal exoskeleton," *IEEE/ASME Trans. Mechatronics*, vol. 21, no. 1, pp. 79–87, Feb. 2016.
- [35] T. Matsubara and J. Morimoto, "Bilinear modeling of EMG signals to extract user-independent features for multiuser myoelectric interface," *IEEE Trans. Biomed. Eng.*, vol. 60, no. 8, pp. 2205–2213, Aug. 2013.
- [36] T. Matsubara, S.-H. Hyon, and J. Morimoto, "Real-time stylistic prediction for whole-body human motions," *Neural Netw.*, vol. 25, pp. 191–199, 2012.
- [37] O. Banerjee, L. E. Ghaoui, and G. Natsoulis, "Convex optimization techniques for fitting sparse Gaussian graphical models," in *Proc. Int. Conf. Mach. Learn.*, 2006, pp. 89–96.
- [38] J. Friedman, T. Hastie, H. Hofling, and R. Tibshirani, "Path wise coordinate optimization," *Annals Appl. Statist.*, vol. 1, pp. 302–332, 2007.



Jun-ichiro Furukawa (M'16) received the B.E. degree in engineering from Osaka University, Osaka, Japan, in 2011, and the M.S. and Ph.D. degrees in engineering from Graduate School of Frontier Biosciences, Osaka University, in 2013 and 2016, respectively.

After receiving the Ph.D. degree, he started working as a Postdoctoral Researcher with the Department of Brain Robot Interface, ATR Computational Neuroscience Laboratories, Kyoto, Japan. His research interests include machine learning, biosignal

processing, computational neuroscience, brain-machine interfaces, and robotics.



Tomoyuki Noda (M'17) received the Ph.D. degree in engineering from Osaka University, Osaka, Japan, in 2009.

In 2009, he joined the Institute for Neural Computation, University California San Diego, San Diego, CA, USA, as a Visiting Research Scholar and, in 2010, started to work as a Postdoc Researcher with ATR Computational Neuroscience Laboratories, Kyoto, Japan.

Dr. Noda received the Best Video Nominate in the IEEE Association for Advancement of Artificial

Intelligence Conference on Artificial Intelligence 2008 and the Best Video in LAB-RS 2008 for the development of a whole body humanoid robot with tactile sensation and compliant joints, and a Best Paper Nominate Award at IEEE Humanoids2012 in BMI controlled Exoskeleton.



Tatsuya Teramae received the Ph.D. degree in engineering from Tottori University, Tottori, Japan, in 2011.

He is a Researcher with the Department of Brain Robot Interface, ATR Computational Neuroscience Laboratories, Kyoto, Japan. His research interests include optimal control and the human machine interface.

Dr. Teramae is a member of the Society of Instrument and Control Engineers in Japan and the Institute of Electrical Engineers of Japan.



Jun Morimoto (M'09) received the Ph.D. degree in information science from Nara Institute of Science and Technology, Nara, Japan, in 2001.

From 2001 to 2002, he was a Postdoctoral Fellow with the Robotics Institute, Carnegie Mellon University, Pittsburgh, PA, USA. Since 2002, he has been at the Advanced Telecommunications Research Institute International, Kyoto, Japan, where he was a Researcher in the Computational Brain Project, the International Cooperative Research Project, Japan Science and Technology Agency from 2004 to 2009.

He is currently the Head of the Department of the Brain Robot Interface, ATR Computational Neuroscience Laboratories, Kyoto. He is IEEE Robotics and Automation Society member.